Dislocation dynamics and surface coarsening of rippled states in the epitaxial growth and erosion on (110) crystal surfaces

Leonardo Golubović[1] and Artem Levandovsky[2]
[1]*Physics Department, West Virginia University, Morgantown, West Virginia 26506-6315, USA*
[2]*Department of Physics and Astronomy, University of California, Riverside, California 92521, USA*
(Received 9 December 2007; published 23 May 2008)

Rippled one-dimensionally periodic structures are commonly seen in the experimental studies of the epitaxial growth and erosion on low symmetry rectangular (110) crystal surfaces. Rippled states period (wavelength) and amplitude grow via a coarsening process that involves motion and annihilations of the dislocations disordering perfect periodicity of these structures. Unlike the ordinary dislocations in equilibrium systems, the dislocations of the growing rippled states are genuinely traveling objects, never at rest. Here, we theoretically elucidate the structure and dynamics of these far-from-equilibrium topological defects. We derive fundamental dislocation dynamics laws that relate the dislocation velocity to the rippled state period. Next, we use our dislocations velocity laws to derive the coarsening laws for the temporal evolution of the rippled state period λ and the ripple amplitude w (surface roughness). For the simple rippled states on (110) surfaces, we obtain the coarsening law $\lambda \sim w \sim t^{2/7}$. Under some circumstances however, we find that these states may exhibit a faster coarsening with $\lambda \sim w \sim t^{1/3}$. We also discuss the dislocations in the rectangular rippled surface states for which we derive the coarsening law with $\lambda \sim w \sim t^{1/4}$. The coarsening laws that occur at the transition from the rippled to the rhomboidal pyramid state are also discussed, as well as the crossover effects that occur in rippled states in the proximity of this transition on (110) crystal surfaces.

DOI: 10.1103/PhysRevE.77.051606 PACS number(s): 81.10.−h, 05.70.Ln, 68.55.−a

I. INTRODUCTION

Structure and dynamics of growing crystal surfaces developing in the epitaxial growth and erosion have attracted a lot of attention over the past decade [1–14]. Due to the Ehrilch-Schwoebel-Villain instability [6], flat crystal surfaces are typically unstable and evolve into growing nanostructures, such as the pyramidal structures that emerge in the homoepitaxial growth on high symmetry (100) and (111) crystal surfaces [1–3,7,8,12]. The most recent and the least explored topic in this area are the intriguing far-from-equilibrium surface morphologies seen in the epitaxial growth [9] and erosion [10,13] on (110) crystal surfaces. These structures have been addressed theoretically only recently [3,16,17]. Unlike the high symmetry (100) and (111) surfaces on which growing pyramidal structures form, on the low symmetry rectangular (110) surfaces, the dominant structures are the so-called rippled states [3,9–11,13,16,17]. They are one-dimensionally periodic surface structures, seen to develop on the (110) crystal surfaces of various materials such as Ag, Cu, and Rh [9,10,13]. The rippled state wave vector points along one of the two principal (high symmetry) directions of the (110) surface. The rippled state surface profile is simply a zigzagged line, i.e., the surface is comprised of long facets, the slope vectors of which alternate from being parallel to being antiparallel to one of the two principal directions of the (110) crystal surface (see Fig. 1). The two principal directions of (110) are not equivalent (symmetry related). Thus, depending on the choice of the preferred direction, there are two major kinds of rippled states: R_1 and R_2 [3,16]. By changing substrate temperature, deposition (or erosion) flux intensity, and molecular beam energy, de Mongeot and coworkers were able to drive the so-called ripple rotation (by 90°) transition between the two kinds of rippled states [9,10,13]. The experiments [9,10,13] as well as the theory [3,16,17] both suggest that this transition is complex and involves the formation of interesting intermediary states intervening between the two rippled states. One of them is the rhomboidal-pyramid (RhP) state that was theoretically predicted in Ref. [3] and subsequently observed in the epitaxial erosion experiments on Rh(110) and Cu(110) surfaces [13]. Alternatively, the ripple rotation transition may proceed through a multistable parameter range, in which both types of the rippled state facets (R_1 and R_2) are locally stable [3,16,17]. This multistable range is realized in the experi-

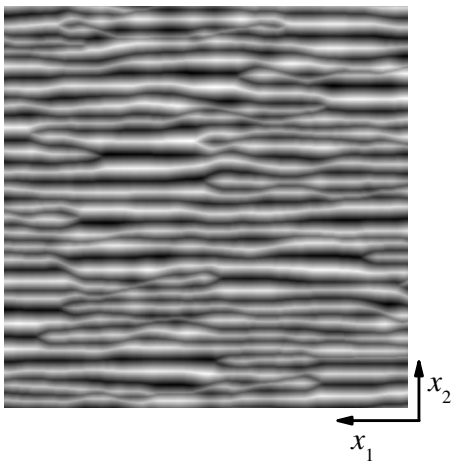

FIG. 1. Contour plot of the (110) surface in the rippled state R_2 (from the simulations discussed in Ref. [16]). Note that ripples have a finite extent along the x_1 direction. Along this direction, the ripples are terminated by dislocation-type topological defects. The presence of the dislocations breaks the perfect periodic order of the rippled state R_2 along the x_2 direction.

ments on the Ag(110) surface, both in the epitaxial growth [9] and in the erosion studies [10]. As theoretically revealed in Refs. [3,16], due to the multistability, the simple rippled states R_1 and R_2 are replaced by more complex rectangular rippled states $R_1^{(\mathrm{rec})}$ and $R_2^{(\mathrm{rec})}$ that are (disordered) checkerboard structures of alternating rectangular pyramids and pits. Unlike the simple R_1 state, a rectangular pyramid of the $R_1^{(\mathrm{rec})}$ state, for example, incorporates not only the long R_1 facets but also significantly smaller metastable R_2 facets [3,16,17]. Rippled rectangular pyramid structures are clearly seen in the scanning tunneling microscope (STM) images from the erosion experiments on Ag(110) [see Fig. 4(d) of Ref. [10]].

In reality, the structures of the simple rippled and rectangular rippled states do not have a long range positional (periodic) order, as evidenced by simulations (see Fig. 1). Experimentally, the lack of the long range positional order is evidenced by a finite width of the correlation peaks seen in the near in-phase surface diffraction data of rippled states [9]. The perfect periodic order is destroyed by the dislocation type topological defects that break the coherence of these structures (see Refs. [3,16] and Fig. 1 here). Due to the dislocations, ripples have only a finite coherence length ξ, corresponding to the typical separation between the dislocations along a ripple [3,16]. Importantly, the simulations show that the rippled state's period λ and the ripple amplitude w ($\sim$ surface roughness) grow via a coarsening process involving motion and annihilations of these dislocations [3,16]. Unlike the dislocations in the standard close-to-equilibrium systems [15], the dislocations of the growing rippled states are genuinely traveling objects never at rest. Over their lifetimes (before they annihilate each other), these dislocations constantly move under the tension of the facet edges terminating at the dislocation core [16].

In this paper, we elucidate the structure and the dynamics of these far-from-equilibrium topological defects. Here, we derive the fundamental dislocation dynamics laws that relate the dislocation velocity to the rippled state period (see Sec. II). Next, in Sec. III, we use our dislocation velocity laws to analytically deduce experimentally interesting surface coarsening laws that govern the temporal evolution of the rippled state period λ, the ripple amplitude ($\sim$ surface roughness) w, and the ripple coherence length ξ. For the simple rippled states, we derive the coarsening laws $\lambda \sim w \sim t^{2/7}$, and $\xi \sim t^{4/7}$, in excellent agreement with the simulations [3,16]. Under some circumstances however, we find that these states may exhibit a faster coarsening, i.e., roughening, with $\lambda \sim w \sim t^{1/3}$ and $\xi \sim t^{1/2}$, also observed in the simulations [16]. We also discuss the dislocations in the rectangular rippled interfacial states for which we analytically derive the coarsening laws $\lambda \sim w \sim t^{1/4}$ and $\xi \sim t^{1/2}$ that have been previously inferred from the simulations [3,16]. The surface coarsening laws at the transition from the rippled to the rhomboidal pyramid state are also discussed, as well as the crossover effects that occur in the proximity of this transition on (110) crystal surfaces.

The layout of this paper is as follows. In Sec. II we derive our dislocation velocity laws. In Sec. III we use these laws to derive the coarsening laws governing surface dynamics of the simple rippled and rectangular rippled states on (110) crystal surfaces. In this section, we discuss the rippled state's coarsening both away and at the transition to the rhomboidal-pyramid state. In Sec. IV, we summarize and discuss our results. In the Appendix, we outline some details from our previous studies which are of direct significance to the theory presented here.

II. KINETIC THEORY OF THE DISLOCATION DYNAMICS IN RIPPLED STATES ON (110) CRYSTAL SURFACES

Our analytic theory of dislocation dynamics is based on the general phenomenological approach to surface dynamics in multilayer epitaxial growth in the absence of (typically weak) adatom desorption and vacancy creation [1–6,16,17]. The deposited film volume is thus conserved. Surface height function $h(\vec{x},t)$ [above the 2D base plane vector $\vec{x}=(x_1,x_2)$] must obey this conservation law. Due to it, the surface velocity $\partial h/\partial t$ can be represented as a divergence of the so-called surface current $\vec{J}=(J_1,J_2)$,

$$\frac{\partial h(\vec{x},t)}{\partial t} = -\vec{\nabla}\cdot\vec{J} = -\frac{\partial J_1}{\partial x_1} - \frac{\partial J_2}{\partial x_2}, \tag{2.1}$$

in the frame comoving with the interface. By the vertical translation symmetry $h \to h+\mathrm{const}$, the surface current $\vec{J}$ can depend only on spatial derivatives of $h(x_1,x_{2,},t)$. The surface current can be decomposed as

$$\vec{J} = \vec{J}^{\mathrm{NE}}(\vec{\nabla}h) + \vec{J}^{\mathrm{curv}}. \tag{2.2}$$

Here, the first term is the so-called surface nonequilibrium current $\vec{J}^{\mathrm{NE}}(\vec{M})$, which is a function of the local surface slope vector $\vec{M}=\vec{\nabla}h=(M_1,M_2)$ only [5]. $\vec{J}^{\mathrm{curv}}$ in Eq. (2.2) is the so-called surface curvature current. This current depends on higher order spatial derivatives of h and vanishes on flat surfaces ("facets") for whatever slope $\vec{M}=\vec{\nabla}h$ they have. It has the form

$$\vec{J}^{\mathrm{curv}} = \vec{J}_{\mathrm{SD}} + \vec{J}_{\mathrm{VA}}. \tag{2.3}$$

Here, $\vec{J}_{\mathrm{SD}} \sim \vec{\nabla}(\nabla^2 h)$ is a contribution isomorphic to the Mullins' surface diffusion current, whereas the $\vec{J}_{\mathrm{VA}}$ in Eq. (2.3) is the so-called vertical asymmetry current discussed in Ref. [17]. $\vec{J}_{\mathrm{VA}}$ current is, by definition, even under vertical reflection, i.e., $\vec{J}_{\mathrm{VA}}(-h)=\vec{J}_{\mathrm{VA}}(+h)$, unlike the other currents involved here ($\vec{J}^{\mathrm{NE}}$ and $\vec{J}_{\mathrm{SD}}$), which are odd (i.e., change sign) under the vertical reflection $h \to -h$ [17]. In our analytic discussion, we will ignore the $\vec{J}_{\mathrm{VA}}$ current and comment on its effects in Sec. IV. We note that curvature currents, such as the surface diffusion current $\vec{J}_{\mathrm{SD}}$, play a significant role on highly curved surface sections such as the edges between facets [see Eqs. (2.8) and (2.9) in the following]. Yet our discussions will in large part rely on the effects of surface nonequilibrium current $\vec{J}^{\mathrm{NE}}(\vec{M})$ on nearly flat (slightly curved) facets on which curvature currents play a subdominant role. The form of the nonequilibrium current $\vec{J}^{\mathrm{NE}}$ in Eq. (2.2) is restricted by reflection symmetries of the (110) surface, which imply the expansion of the form [3,16]

$$J_1^{\mathrm{NE}}(M_1,M_2) = M_1[r_1 - u_{11}M_1^2 - u_{12}M_2^2 + \cdots],$$

$$J_2^{\mathrm{NE}}(M_1,M_2) = M_2[r_2 - u_{22}M_2^2 - u_{21}M_1^2 + \cdots]. \quad (2.4)$$

The ellipses in Eq. (2.4) indicate higher order terms, which will be truncated out in the following. This yields the simplest possible yet comprehensive model consistent with the symmetries of (110) surface. The model has a rich and experimentally interesting kinetic phase diagram involving simple rippled, rhomboidal-pyramid (RhP), buckled-rippled ($R^{(\mathrm{buc})}$), and rectangular rippled ($R^{(\mathrm{rec})}$) surface states [3,16,17]. See the Appendix for an outline of this phase diagram. Here we note that there are two major types of the phase behaviors predicted by this phase diagram: (i) Type A behavior (occurring in systems with $u_{11}u_{22} > u_{12}u_{21}$), in which the RhP or $R^{(\mathrm{buc})}$ states intervene between the rippled states R_1 and R_2. (ii) Type B behavior (occurring in systems with $u_{11}u_{22} < u_{12}u_{21}$), in which the $R^{(\mathrm{rec})}$ states intervene between the rippled states R_1 and R_2. In experiments, the type B behavior was observed on a Ag(110) surface [9,10]. The type A behavior, predicted in Ref. [3], was subsequently also observed, on the Rh(110) and Cu(110) surfaces [13].

For the special case $u_{12}=u_{21}=u$, the $\vec{J}^{\mathrm{NE}}(\vec{M})$ Eq. (2.4) becomes a gradient of a potential

$$\vec{J}^{\mathrm{NE}}(\vec{M}) = -\frac{\partial U(\vec{M})}{\partial \vec{M}}, \quad (2.5a)$$

with the potential

$$U(M) = -\frac{r_1}{2}M_1^2 - \frac{r_2}{2}M_2^2 + \frac{u_{11}}{4}M_1^4 + \frac{u}{2}M_1^2M_2^2 + \frac{u_{22}}{4}M_2^4, \quad (2.5b)$$

whereas the interface dynamics Eq. (2.1) can be shown to be equivalent to

$$\frac{\partial h(x,t)}{\partial t} = -\frac{\delta F_{\mathrm{eff}}}{\delta h(x,t)}. \quad (2.6a)$$

Here, F_{eff} is an effective free energy functional of the form $F_{\mathrm{eff}}(h)=F_{\mathrm{NE}}+F_{\mathrm{SD}}$, with

$$F_{\mathrm{NE}} = \int d^2x U(\vec{M}(\vec{x})), \quad (2.6b)$$

contributing the nonequlibrium current $\vec{J}^{\mathrm{NE}}(\vec{M})$ to Eq. (2.2), i.e., to Eq. (2.1), and

$$F_{\mathrm{SD}} = \int d^2x \left[\frac{\kappa_{11}}{2}\left(\frac{\partial^2 h}{\partial x_1^2}\right)^2 + \kappa_{12}\left(\frac{\partial^2 h}{\partial x_1\,\partial x_2}\right)^2 + \frac{\kappa_{22}}{2}\left(\frac{\partial^2 h}{\partial x_2^2}\right)^2 \right] \quad (2.6c)$$

contributing the surface diffusion $\vec{J}_{\mathrm{SD}}$ to Eq. (2.3), i.e., to Eqs. (2.2) and (2.1). We stress that for $u_{12} \neq u_{21}$ there is no F_{eff} that would generate dynamics via Eq. (2.6a). A major aspect of the epitaxial growth is the selection of the slope vectors of the faceted morphologies developing across the growing surface. The selected facet slope vectors are commonly assumed to correspond to the zeros of $\vec{J}^{\mathrm{NE}}(\vec{M})$. There are, however, known exceptions to this "zero current rule" [16]. In fact, this rule necessarily holds for the surface dynamics governed by an effective free energy: By Eqs. (2.5) and (2.6) it can be shown that

$$\frac{dF_{\mathrm{eff}}}{dt} = -\int d^2x \left(\frac{\partial h}{\partial t}\right)^2 \leq 0, \quad (2.7)$$

i.e., F_{eff} generally decreases in time. This is achieved by breaking up of the interface into nearly flat *growing* facets: on a flat facet the surface diffusion "free energy" $F_{\mathrm{SD}} \geq 0$, Eq. (2.6c) reduces to zero, whereas the nonequilibrium current free energy Eq. (2.6b) is minimized by selecting the slopes that minimize the local potential $U(\vec{M})$. Thus, by Eq. (2.5a), $\vec{J}^{\mathrm{NE}}=0$ at the slope vectors of the selected facets. The effective free energy *in excess* of the absolute minimum is localized in the *edges* between the selected facets. An edge of the length l contributes the excess effective free energy proportional to its length,

$$\Delta F_{\mathrm{eff}} = \sigma l. \quad (2.8)$$

During the surface coarsening process, the facets grow so the total length of the present edges decreases in time, yielding a decrease of F_{eff}, in accord with Eq. (2.7). In Eq. (2.8), σ is the edge line tension, which can be easily calculated for static edges ($\partial h/\partial t=0$) between facets (see Ref. [1]). For example, for the static edges occurring in the rippled state R_2 we obtain, by using Eqs. (2.1)–(2.5),

$$\sigma = \frac{2\sqrt{2\kappa_{22}}(r_2)^{3/2}}{3u_{22}}, \quad (2.9)$$

for the edge between the R_2 facet with $(M_1=0, M_2=+M_0)$ and the R_2 facet with $(M_1=0, M_2=-M_0)$. Here, $M_0=(r_2/u_{22})^{1/2}$. We outline the derivation of Eq. (2.9) at the end of the Appendix to this paper. We note that, in our model, unless $u_{12}=u_{21}$, there is *no* F_{eff} governing the interface dynamics. Thus, for $u_{12} \neq u_{21}$, it is *not* assured that interface structures have facets vanishing $\vec{J}^{\mathrm{NE}}(\vec{M})$. This is evidenced by the existence of the so-called buckled-rippled state, which indeed exhibits persistent surface currents [3,16]. Still, with this important exception, numerical simulations [3,16] indicate that for all other states present in our model [Eqs. (2.1)–(2.4)] the selected facet slopes $\vec{M}$ are zeros of $\vec{J}^{\mathrm{NE}}(\vec{M})$ even for $u_{12} \neq u_{21}$.

The basic structure of a single dislocation close to its core is shown in Fig. 2 for the case of the R_2 rippled state with the half-period=λ. The dislocations of a rippled state travel (glide) along the ripples, i.e., their velocities are perpendicular to the wave vector of the rippled state periodic structure [3,16]. Figure 2(a) gives a surface section around a dislocation, whereas in Fig. 2(b) we depict the dislocation in terms of the edges between facetlike surface sections seen in Fig. 2(a). The dislocation moves to the right in Fig. 2(b). As revealed by the simulations in Refs. [3,16], this dislocation motion is essential for the overall surface dynamics. It is the primary mechanism of the rippled state surface coarsening: As the dislocation in Fig. 2 moves to the right, the two facets of the width λ (above and below the middle facet) merge to

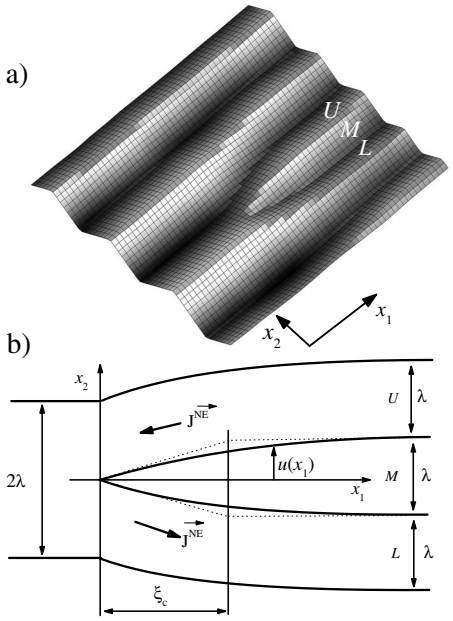

FIG. 2. In (a), 3D view of a surface section containing a dislocation in the simple rippled state R_2 (from the simulations discussed in Ref. [16]). In (b), the dislocation is depicted in terms of the edges between facetlike surface sections seen in (a). The dislocation is comprised of three R_2 facets: flat middle facet (M) having a knifelike shape, and upper (U) and lower (L) facets, which are both slightly curved mostly along the x_1 direction.

form the larger facet of the width 2λ. These two facets, labeled in Fig. 2 as "upper" (U) and "lower" (L) facets [relative to the "middle" (M) facet in Fig. 2], play an essential role in the following discussions. In the following, we address the structure and dynamics of these dislocations. In particular, we derive the kinetic law $v(\lambda)$ relating the dislocation velocity v to the phase half-period λ. This law is essential for obtaining the surface coarsening laws, which are pursued in Sec. III.

As the first step in this direction, we elucidate the dislocation core geometry in Fig. 2. It depicts the so-called knife dislocation of the rippled surface state [16]. For the dislocation in Fig. 2, the interface profile is odd in x_2, $h(x_1,-x_2)=-h(x_1,x_2)$, in the coordinate system (x_1,x_2) indicated in Fig. 2(b). For $x_1>0$, the middle knifelike facet [the M facet occurring for $|x_2|<u(x_1)$ in Fig. 2(b)] is flat, i.e., it is an R_2 facet, with

$$h_{\text{middle}}(x_1,x_2)=M_0x_2. \tag{2.10}$$

The facet above the middle facet [the "upper facet" U in Fig. 2(b)] is weakly curved in the core region, with the profile of the form

$$h_{\text{upper}}(x_1,x_2,t)=M_0\frac{\lambda}{2}-M_0\left(x_2-\frac{\lambda}{2}\right)+\delta h(x_1,x_2,t). \tag{2.11}$$

Here, the last term $\delta h\to 0$ as $x_1\to+\infty$, so in this limit the edge between the middle and the upper facet is located at $x_2=\lambda/2$ [see Fig. 2(b)]. The edge shape $u(x_1)$ in Fig. 2(b) can be found by noting that along the edge the surfaces in Eqs. (2.10) and (2.11) intersect, i.e.,

$$h_{\text{middle}}(x_1,x_2=u(x_1))=h_{\text{upper}}(x_1,x_2=u(x_1),t).$$

This condition and Eqs. (2.10) and (2.11) yield the equation

$$u(x_1,t)=\frac{\lambda}{2}+\frac{\delta h(x_1,x_2=u(x_1,t),t)}{2M_0}. \tag{2.12}$$

For a given form of $\delta h(x_1,x_2,t)$, Eq. (2.12) can be solved for the edge shape $u(x_1,t)$. As discussed in the following, the dislocation core becomes sharp at long times, with λ (core length scale along x_2) much smaller than the core lateral size ξ_c (core length scale along x_1) in Fig. 2(b). Due to this, the x_2 dependence of δh in Eq. (2.11) can be ignored relative to its x_1 dependence. In the absence of the x_2 dependence, the surface slope vector field $\vec{M}=\vec{\nabla}h=(\partial h/\partial x_1,\partial h/\partial x_2)=(M_1,M_2)$ of the upper facet in Fig. 2(b) is simply

$$M_1(x_1,t)=\frac{\partial}{\partial x_1}\delta h(x_1,t),\quad M_2=-M_0, \tag{2.13}$$

whereas, by Eq. (2.12), the edge profile is directly found as

$$u(x_1,t)=\frac{\lambda}{2}+\frac{\delta h(x_1,t)}{2M_0}. \tag{2.14}$$

As $\delta h(x_1,t)\to 0$ for $x_1\to\infty$, one has $u(x_1,t)\to\lambda/2$ in this limit. On the other hand, by Fig. 2(b), $u(x_1,t)$ vanishes at the very dislocation core. So, by Eq. (2.14), $\delta h=-M_0\lambda$ at the core. By combining these two facts with Eq. (2.13), we find

$$\int_{x_c}^{\infty}dx_1M_1(x_1,t)=M_0\lambda, \tag{2.15}$$

for the core located at $x_1=x_c$. Hereafter, we discuss a steadily traveling dislocation, with the dislocation core translating along the x_1 axis with constant velocity v. For such a dislocation, the core position $x_c(t)=vt$, and $\delta h(x_1,t)=\delta h(x_1-vt)$. Thus, also, $M_1(x_1,t)=M_1(x_1-vt)=M_1(X_1)$ [with $X_1=x_1-x_c(t)=x_1-vt$], whereas

$$\frac{\partial}{\partial t}\delta h=-v\frac{\partial}{\partial x_1}\delta h=-vM_1. \tag{2.16}$$

As $\vec{J}^{\text{NE}}(\vec{M})$ is only x_1 dependent, Eq. (2.1) reduces to $\partial h/\partial t=-\partial J_1/\partial x_1$. This and Eqs. (2.16) and (2.13) yield

$$-vM_1(X_1)=-\frac{d}{dX_1}J_1^{(\text{NE})}(M_1(X_1),M_2=M_0). \tag{2.17}$$

For a given form of $J_1^{\text{NE}}(M_1,M_2)$, the differential Eq. (2.17) can be solved for the slope $M_1(X_1)$ of the upper moving facet and, eventually, the edge profile $u(x_1)$ in Fig. 2 can then be extracted by means of Eq. (2.14). In the practically interesting limit $\xi_c\gg\lambda$ (see the following), the upper and lower facets in Fig. 2(b) are only weakly curved. Thus, the curvature surface currents in Eq. (2.2) could have been ignored, as tacitly done in deriving Eq. (2.17) above. In this limit, the surface nonequilibrium current $\vec{J}^{\text{NE}}(\vec{M})$ plays the dominant role in determining the shape of the "traveling" facets, such as the upper (U) and lower (L) facets in Fig. 2(b). In this

figure, on the middle (M) flat facet $\vec{J}^{\rm NE}=0$, whereas the upper and lower facets both move due to a nonzero downhill current that displaces the material from the upper facet [there, $\vec{J}^{\rm NE}$ flows to the left in Fig. 2(b)] to the lower facet [there, $\vec{J}^{\rm NE}$ flows to the right in Fig. 2(b)]. Importantly, note that this removal of the material from the upper facet and its subsequent absorption on the lower facet causes the dislocation to move to the right in Fig. 2(b). To obtain the dislocation velocity v from this physical picture, we integrate both sides of Eq. (2.17) over the range $0<X_1<\infty$ [corresponding to $x_c<x_1<\infty$] to obtain

$$-v\int_0^\infty dX_1 M_1(X_1) = -J_1^{\rm NE}(M_1=0,M_2=M_0) + J_1^{\rm NE}(M_1=M_1(0),M_2=M_0) = +J_1^{\rm NE}(M_1=M_1(0),M_2=M_0). \tag{2.18}$$

Here, we used the fact that the preferred R_2 slope $(M_1=0,M_2=M_0)$, having $\vec{J}^{\rm NE}=0$, is reached for $x_1\to\infty$. By Eqs. (2.18) and (2.15)),

$$M_0 v\lambda = -J_1^{\rm NE}(M_1(0),M_0). \tag{2.19}$$

For a given λ, Eq. (2.19) relates the dislocation velocity v to the slope component $M_1(0)$ of the upper facet at the dislocation core position $X_1=0$ in Fig. 2(b). $M_1(0)$ is directly related to the knife dislocation sharpness, i.e., its aspect ratio λ/ξ_c. Indeed, by Fig. 2(b), and Eqs. (2.14) and (2.13),

$$\frac{\lambda/2}{\xi_c} \cong \left.\frac{du}{dX_1}\right|_{X_1=0} = \frac{M_1(0)}{2M_0}. \tag{2.20}$$

Thus, the dislocation aspect ratio is

$$\frac{\lambda}{\xi_c} \cong \frac{M_1(0)}{M_0}. \tag{2.21}$$

Equation (2.21) will be used in the following to show that the dislocation aspect ratio becomes small in the interesting limit of large λ [see Eq. (2.28b) in the following]. Due to this, as evidenced also by our simulation in Refs. [3,16], the dislocations get sharper and sharper as the coarsening process goes on. In addition to the dislocation motion, the interface coarsening involves also the processes of dislocation annihilations, as qualitatively discussed in Refs. [3,16]. Due to the annihilations, the dislocations ensemble becomes dilute at long times, i.e., the distances between neighboring dislocations become large. For dilute dislocation systems, it is sufficient to consider just a single dislocation system in order to obtain its velocity v and the aspect ratio $\lambda/\xi_c=M_1(0)/M_0$ as functions of λ. To accomplish this we need one more [in addition to Eq. (2.19)] relation between these three fundamental characteristics of the traveling dislocations. This relation can be obtained by applying Eq. (2.7) to the single dislocation system depicted in Fig. 2. In the single dislocation system, over the time dt, the length of each of the *two* edges terminating at the dislocation core in Fig. 2(b) shortens by the length $dl=vdt$. This yields the change of the net effective free energy $dF_{\rm eff}=-2\sigma dl=-2\sigma v dt$, with σ, the edge line tension; see Eqs. (2.8) and (2.9). Thus, by Eq. (2.7),

$$-2\sigma v = -\int dx_2 \int dx_1 \left(\frac{\partial h}{\partial t}\right)^2. \tag{2.22}$$

Here, $\partial h/\partial t\neq 0$ only on the surfaces of the upper and lower traveling facets in Fig. 2(b). These two facets [each of the width $\int dx_2=\lambda$] equally contribute to the right-hand side of Eq. (2.22), which thus reduces to

$$-2\sigma v = -2\lambda\int_{x_c}^\infty dx_1 \left(\frac{\partial h}{\partial t}\right)^2.$$

Using here Eq. (2.16), we obtain

$$\sigma v = \lambda\int_{x_c}^\infty dX_1 (vM_1(X_1))^2. \tag{2.23}$$

Equations (2.23) and (2.19) constitute our two fundamental laws of the dislocation dynamics. We will use them here to obtain the dislocation velocity v and its aspect ratio $\lambda/\xi_c=M_1(0)/M_0$ as functions of λ, i.e., of the rippled state period. Prior to this, we note that, as $M_1(X_1)\approx M_1(0)$ for $X_1<\xi_c$ and $M_1(X_1)\approx 0$ for $X_1>\xi_c$, Eq. (2.23) implies the scaling relation $\sigma v\sim\lambda\xi_c(vM_1(0))^2$. Thus,

$$v = \text{const}\frac{\sigma}{\lambda\xi_c(M_1(0))^2}, \tag{2.24a}$$

so, by Eq. (2.21),

$$v = \text{const}\frac{\sigma\xi_c}{(M_0)^3\lambda^3} \sim \frac{\xi_c}{\lambda^3}. \tag{2.24b}$$

Equation (2.24b) can be easily combined with Eq. (2.19) to reach several important conclusions on the dislocation structure and dynamics. The surface current entering Eq. (2.19) is, by Eq. (2.4),

$$-J_1(M_1(0),M_0) = \tilde{T}_{11}M_1(0) + u_{11}M_1^3(0), \tag{2.25}$$

with

$$\tilde{T}_{11} = -r_1 + u_{12}M_0^2 = -r_1 + u_{12}r_2/u_{22}. \tag{2.26}$$

$\tilde{T}_{11}$ defined in Eq. (2.26) is positive within the stability range of the rippled phase R_2. $\tilde{T}_{11}$ vanishes at the rippled to rhomboidal-pyramid (R_2-to-RhP) state transition, as well as at the rippled to buckled-rippled (R_2-to-$R^{(\rm buc)}$) state transition; see the Appendix to this paper. Away from the transition ($\tilde{T}_{11}\neq 0$), one can ignore the $[M_1(0)]^3$ term in Eq. (2.25) with no qualitative consequences [as justified in the following]. So, for $\tilde{T}_{11}\neq 0$,

$$-J_1(M_1(0),M_0)\sim M_1(0),$$

and thus, by Eqs. (2.19) and (2.21),

$$v\lambda \sim \frac{M_1(0)}{M_0} = \frac{\lambda}{\xi_c}. \tag{2.27}$$

Thus, the dislocation velocity $v \sim 1/\xi_c$. This fact is easily combined with the scaling relation Eq. (2.24b) to reach the following conclusions: For $\tilde{T}_{11} \neq 0$, the dislocation velocity scales as

$$v \sim \frac{1}{\xi_c} \sim \frac{1}{\lambda^{3/2}}, \tag{2.28a}$$

whereas the dislocation aspect ratio scales as

$$\frac{M_1(0)}{M_0} \sim \frac{\lambda}{\xi_c} \sim \lambda v \sim \frac{1}{\lambda^{1/2}}. \tag{2.28b}$$

We note that the prefactor of the power law in Eq. (2.28a) can also be calculated as done later on in this section [see Eq. (2.39)]. Equation (2.28a) will be used in Sec. III to discuss the coarsening dynamics of the rippled states on (110) surfaces. By Eq. (2.28a),

$$\xi_c \sim \lambda^{3/2}. \tag{2.28c}$$

Thus, the dislocation aspect ratio $\lambda/\xi_c \sim 1/\lambda^{1/2}$ becomes small, i.e., dislocations become very sharp in the significant limit of large λ [which is reached at long times (see Sec. III)]. In this limit, $M_1(0)$ approaches zero [see Eq. (2.28b)]. Due to this fact, in the above discussion it was appropriate to ignore the term $\sim[M_1(0)]^3$ and keep the term $\sim M_1(0)$ in Eq. (2.25), for $\tilde{T}_{11} \neq 0$.

On the other hand, at the R_2-to-RhP transition ($\tilde{T}_{11}=0$), by Eq. (2.25), $-J_1(M_1(0), M_0) \sim (M_1(0))^3$, and thus, by Eq. (2.19),

$$v\lambda \sim (M_1(0))^3 \sim (\lambda/\xi_c)^3. \tag{2.29}$$

Combining the scaling relations in Eqs. (2.29) and (2.24b) yields

$$v \sim \frac{1}{\lambda^{7/4}} \tag{2.30a}$$

and

$$\frac{M_1(0)}{M_0} \sim \frac{\lambda}{\xi_c} \sim \frac{1}{\lambda^{1/4}} \tag{2.30b}$$

at the rippled-to-RhP state transition. The prefactor of the power law in Eq. (2.30a) is calculated later on in this section [see Eq. (2.38)].

By comparing the two different velocity laws in Eqs. (2.30a) and (2.28a), we see that for a given large λ, the dislocations are typically slower at the rippled-to-RhP transition than away from it. This yields a slower surface coarsening at the transition, with a distinct set of coarsening exponents discussed in Sec. III. This phenomenon has been evidenced also in our simulations in Ref. [16]. It is manifested through a significant depression of the interface roughness that occurs at the R_2-to-RhP transition. See Ref. [16] and Fig. 5(b) therein at $a=a_-$. Here,

$$a = \frac{r_1/\sqrt{u_{11}} - r_2/\sqrt{u_{22}}}{r_1/\sqrt{u_{11}} + r_2/\sqrt{u_{22}}},$$

and

$$a_- = -\frac{1 - u_{12}/\sqrt{u_{11}u_{22}}}{1 + u_{12}/\sqrt{u_{11}u_{22}}}.$$

a is a dimensionless system parameter introduced in Refs. [3] and [16]; see also the Appendix to this paper. As detailed in the Appendix, the quantity $\tilde{T}_{11}$ defined above in Eq. (2.26) is proportional to the difference $a_- - a$. Thus, the condition $a=a_-$ corresponds to the R_2-to-RhP (or the R_2-to-$R^{(\mathrm{buc})}$) transition point at which $\tilde{T}_{11} \sim a_- - a$ vanishes. Away but close to this transition, there is a prominent crossover from the behavior in Eq. (2.28) to the behavior in Eq. (2.30), which is especially significant for small nonzero values of $\tilde{T}_{11} \sim a_- - a > 0$. In the simulations of Ref. [16], this crossover manifests itself through a significant depression of the interface width (roughness) that occurs in the proximity of the R_2-to-RhP transition; see Fig. 5(b) of Ref. [16].

To analyze this crossover phenomenon quantitatively, and also to derive the prefactors (amplitudes) of the power laws in Eqs. (2.28a) and (2.30a), we reexpress the dislocation dynamics law in Eq. (2.23) by changing the integration over X_1 into an integration over M_1. It can be done using Eq. (2.17) which implies

$$vM_1 = \frac{\partial J_1(M_1, M_0)}{\partial M_1}\frac{dM_1}{dX_1}. \tag{2.31}$$

Thus,

$$dX_1 = \frac{1}{vM_1}\frac{\partial J_1(M_1, M_0)}{\partial M_1} dM_1. \tag{2.32}$$

By Eq. (2.32), our Eq. (2.23) can be transformed into

$$\frac{\sigma}{\lambda} = -\int_0^{M_1(0)} dM_1 M_1 \frac{\partial J_1(M_1, M_0)}{\partial M_1}. \tag{2.33}$$

For a given form of $J_1(M_1, M_0)$, the integral in Eq. (2.33) can be explicitly calculated. Thus, by Eq. (2.4),

$$\frac{\sigma}{\lambda} = \frac{1}{2}\tilde{T}_{11}(M_1(0))^2 + \frac{3}{4}u_{11}(M_1(0))^4. \tag{2.34}$$

Equation (2.34) enables one to calculate $M_1(0)$ directly for a given λ. In addition, by Eqs. (2.19) and (2.25), we also have

$$M_0 v\lambda = \tilde{T}_{11}M_1(0) + u_{11}(M_1(0))^3. \tag{2.35}$$

The biquadratic Eq. (2.34) can be analytically solved for $M_1(0)$, and, furthermore, this solution can be inserted into Eq. (2.35). Eventually, this yields a closed expression for the dislocation velocity v as a function of λ. There is no need for us to exhibit here this lengthy formula, since the basic features significant for the aforementioned crossover are clear already from the structure of Eqs. (2.34) and (2.35). At the aforementioned crossover, the $M_1(0)$ assumes a characteristic value M_{cross} that can be simply obtained by balancing the

first with the second term in Eqs. (2.34) and (2.35). Thus, the crossover occurs when $\tilde{T}_{11} \approx u_{11}(M_1(0))^2$, i.e., for

$$M_1(0) \approx M_{\text{cross}} = (\tilde{T}_{11}/u_{11})^{1/2}. \tag{2.36}$$

By Eq. (2.34), this corresponds to the crossover value of λ of the form

$$\lambda_{\text{cross}} \approx \frac{\sigma}{\tilde{T}_{11}(M_{\text{cross}})^2} \approx \frac{\sigma}{u_{11}(M_{\text{cross}})^4} \sim \frac{1}{(\tilde{T}_{11})^2} \sim \frac{1}{(a_- - a)^2}. \tag{2.37}$$

Next, by Eqs. (2.34) and (2.35), for $\lambda \ll \lambda_{\text{cross}}$, i.e., $M_1(0) \gg M_{\text{cross}}$,

$$v(\lambda) = \left(\frac{4}{3}\right)^{3/4} \frac{u_{11}^{1/4}\sigma^{3/4}}{\lambda^{7/4}} \sim \frac{1}{\lambda^{7/4}}. \tag{2.38}$$

Thus, for $\lambda \ll \lambda_{\text{cross}}$ one has the scaling behavior seen at the ripple-to-RhP state transition, Eq. (2.30a). On the other hand, for $\lambda \gg \lambda_{\text{cross}}$, i.e., $M_1(0) \ll M_{\text{cross}}$, by Eqs. (2.34) and (2.35),

$$v(\lambda) = \frac{(2\sigma\tilde{T}_{11})^{1/2}}{M_0\lambda^{3/2}} \sim \frac{(\tilde{T}_{11})^{1/2}}{\lambda^{3/2}} \sim \frac{(a_- - a)^{1/2}}{\lambda^{3/2}}. \tag{2.39}$$

Thus, for $\lambda > \lambda_{\text{cross}}$ one has the ultimate scaling behavior seen off the transition critical point, Eq. (2.28a). As this transition point is approached, λ_{cross} diverges, and one is left with the purely critical scaling behavior in Eq. (2.38), i.e., Eq. (2.30). In Sec. III, we discuss the effects of this significant crossover on the overall surface coarsening dynamics.

It should not escape ones attention that in the above discussions we restricted ourselves to the case when the effective free energy functional F_{eff} generating the surface dynamics exists. As discussed earlier in this section, the existence of F_{eff} strictly requires that $u_{21}=u_{12}$ in the expressions giving the nonequilibrium current components, Eq. (2.4). Yet, we will argue here that this restriction is irrelevant, so our basic results such as the dislocation velocity scaling laws $v(\lambda)$ in Eq. (2.38) [i.e., Eq. (2.30a)] and Eq. (2.39) [i.e., Eq. (2.28a)] remain valid even for $u_{21} \neq u_{12}$. Indeed, note that u_{21} enters the current component J_2^{NE}, which is actually *absent* in any of the equations displayed in our derivations here [such as the basic equation (2.17)]. Due to this, the actual value of u_{21} is irrelevant. Thus, for any $u_{21} \neq u_{12}$ one has the same scaling behavior $v(\lambda)$ as for $u_{21}=u_{12}$.

III. COARSENING DYNAMICS OF RIPPLED STATES ON (110) SURFACES

As evidenced by our simulations in Refs. [3] and [16], the coarsening growth of rippled state period λ is meditated by traveling dislocations [with velocity $v(\lambda)$], in a way similar to the one discussed before by Moldovan and Golubović (Ref. [1], denoted as MG in the following), for the pyramidal states on (100) surfaces. In fact, (100) surfaces coarsen by the gliding motion and annihilations of two nearly independent dislocations ensembles, moving along the two principal (perpendicular to each other) axes of the (100). That is, the dislocations of one of the ensembles move along the direction of one of the principal axes while the dislocations of the other ensemble move along the direction of the other principal axis. It has been found, in the MG study of (100) surfaces, that the dislocations from different ensembles occasionally collide and form bound pairs. However, these dislocation bound states are short lived and eventually decay. Thus, the two dislocation ensembles are nearly decoupled from each other and they independently (and simultaneously) contribute to the (100) surfaces coarsening. Geometrically, *each* of these two dislocation ensembles on (100) surfaces is equivalent to the rippled state dislocation ensemble on (110) surfaces seen in Fig. 1 here. Due to this, a few of the basic (geometric in origin) relations for the growth kinetics of the surface state period λ can be adopted here from MG (see Sec. VIII of Ref. [1]). These are: (i) the relation

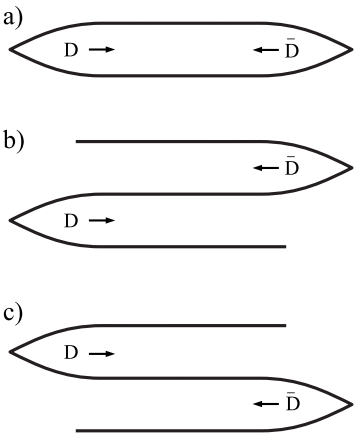

FIG. 3. Facet edges plots depicting the three channels for the annihilation of a rippled state dislocation D (moving here to the right) with an antidislocation (moving to the left): The channel in (a) is realized for the dislocation and antidislocation having cores on the same facet, and in the channels (b) and (c) the cores of the dislocation and the dislocation are on the nearest-neighbor facets.

$$\frac{1}{\lambda}\frac{d\lambda}{dt} = \frac{2v(\lambda)}{\xi(\lambda)}, \tag{3.1}$$

with ξ, the separation between dislocations along a ripple (see Refs [16] and [1]), and (ii) the relation

$$\xi \sim \lambda^{q-1}, \tag{3.2}$$

with $q=3$, the number of channels for dislocation annihilations, that is, the number of distinct ways for an annihilation to proceed by having only continuous changes of the edges network [1]. In Fig. 3, we depict the facet edges plots corresponding to these three channels for the annihilation of a rippled state dislocation D (moving to the right in the figure) with an antidislocation (moving to the left): The channel in Fig. 3(a) corresponds to the annihilation of D with an antidislocation the core of which is on the same facet as the core of D. For the channels in Figs. 3(b) and 3(c), the cores of the dislocation and the antidislocation are on the nearest-neighbor facets. Thus, there is a total of $q=3$ channels for dislocations annihilations which are allowed by the requirement of having only continuous changes of the edges net-

works of rippled states. As discussed by Moldovan and Golubović in Ref. [1], the dislocations of pyramidal states on (100) surfaces also have $q=3$ channels for their annihilations. This fact simply reflects the above noted geometrical relation of the (100) surface dislocation ensembles to the rippled state dislocations ensemble discussed in this study on (110) surfaces.

The major qualitative difference between the dislocations of the four-sided pyramidal states on (100) surfaces, discussed in MG, and those of the rippled states discussed here in Sec. II, is in their velocity law $v(\lambda)$. This difference affects the detailed form of the coarsening law giving the growth of $\lambda(t)$ vs time. By Eqs. (3.1) and (3.2), this growth law can be extracted from

$$t = \int_0^{\lambda(t)} \frac{d\lambda}{\lambda} \frac{\xi(\lambda)}{v(\lambda)} \sim \int_0^{\lambda(t)} \frac{d\lambda}{\lambda} \frac{\lambda^{q-1}}{v(\lambda)}. \tag{3.3}$$

Equation (3.3) can be combined with the dislocation velocity laws $v(\lambda)$ we derived in Sec. II, to obtain the coarsening laws governing the dynamics of rippled states on (110) surfaces. For this purpose, we note that for the power-law velocity laws of the form

$$v(\lambda) \sim \frac{1}{\lambda^{n_v}}, \tag{3.4}$$

Eq. (3.3) is easily shown to imply the coarsening laws,

$$\lambda(t) \sim t^{n_\lambda}, \quad \xi(t) \sim t^{n_\xi}, \tag{3.5}$$

with

$$n_\lambda = \frac{1}{q-1+n_v}, \tag{3.6}$$

and

$$n_\xi = (q-1)n_\lambda = \frac{q-1}{q-1+n_v}. \tag{3.7}$$

In the presence of the crossover discussed at the end of Sec. II, $v(\lambda)$ is not a simple power law as in Eq. (3.4). Thus, in general, Eq. (3.3) needs to be combined with the results of Sec. II [see Eqs. (2.34) and (2.35)] to derive the actual growth law of $\lambda(t)$. Since $v(\lambda)$ has power-law asymptotic forms on both sides of the crossover, the crossover behavior of $v(\lambda)$ vs λ directly implies corresponding crossover behavior of $\lambda(t)$ (and of $\xi(t) \sim [\lambda(t)]^{q-1}$) vs time t. This crossover occurs at a characteristic time scale $t_{\rm cross}$ at which $\lambda(t_{\rm cross}) = \lambda_{\rm cross}$, with $\lambda_{\rm cross}$ as in Eq. (2.37). By the results of Sec. II, one thus expects two scaling behaviors, one for $t \ll t_{\rm cross}$ [corresponding to $\lambda(t) \ll \lambda_{\rm cross}$] and the other one for $t \gg t_{\rm cross}$ [corresponding to $\lambda(t) \gg \lambda_{\rm cross}$]. The crossover time scale $t_{\rm cross}$ can be easily obtained by combining Eq. (3.3) with Eqs. (2.37) and (2.38). Thus, we find

$$t_{\rm cross} \sim \frac{1}{(\tilde{T}_{11})^{2q+3/2}} = \frac{1}{(\tilde{T}_{11})^{15/2}}, \tag{3.8}$$

which diverges at the ripple-to-RhP state transition point because $\tilde{T}_{11} \sim a_- - a$ vanishes at this transition. For $t \ll t_{\rm cross}$, one has $\lambda \ll \lambda_{\rm cross}$, and $v(\lambda)$ is as in Eq. (2.30a) [i.e., Eq. (2.38)], corresponding to Eq. (3.4) with the velocity exponent $n_v = 7/4$. With this value of n_v, by Eqs. (3.6) and (3.7), with $q=3$ (see MG), we find that $w(t) \sim \lambda(t) \sim t^{n_\lambda}$ and $\xi \sim t^{n_\xi}$, with

$$n_\lambda = \frac{4}{15} \cong 0.2666, \quad n_\xi = \frac{8}{15}, \tag{3.9}$$

for $t \ll t_{\rm cross}$. At the ripple-to-RhP transition ($\tilde{T}_{11}=0$), the crossover time Eq. (3.8) is infinite, and the coarsening with the exponents in Eq. (3.9) persists at arbitrarily long times. Off this transition ($\tilde{T}_{11}>0$), in the rippled phase, $t_{\rm cross}$ is finite, and for $t \gg t_{\rm cross}$, one has $\lambda(t) \gg \lambda_{\rm cross}$, and $v(\lambda)$ is as in Eq. (2.28a) [i.e., Eq. (2.39)] corresponding to the Eq. (3.4) with the velocity exponent $n_v = 3/2$. With this value of n_v, by Eqs. (3.6) and (3.7), with $q=3$ (see MG), we find $w \sim \lambda \sim t^{n_\lambda}$ and $\xi \sim t^{n_\xi}$, with

$$n_\lambda = \frac{2}{7} \cong 0.2857, \quad n_\xi = \frac{4}{7}. \tag{3.10}$$

In fact, by Eqs. (2.39) and (3.3), we find, for $t \gg t_{\rm cross}$,

$$w(t) \sim \lambda(t) \sim (\tilde{T}_{11})^{1/7} t^{2/7} \sim (a_- - a)^{1/7} t^{2/7}, \tag{3.11}$$

indicating that the amplitude of this coarsening law vanishes at the R_2-to-RhP transition. At the very transition point, the coarsening in Eq. (3.11) is pushed away to infinite times and, by Eq. (3.9), replaced by the slower coarsening law $w(t) \sim \lambda(t) \sim t^{4/15}$. Away from the transition point, this critical coarsening behavior persists up times $= t_{\rm cross}$ where it crosses over to the coarsening law in Eq. (3.11), with a bigger coarsening exponent $n_\lambda = 2/7 \cong 0.2857$. This coarsening exponent is in excellent agreement with the value obtained from the rippled state simulations in Refs. [3,16], away from the transition point. Also, these simulations indicate that the amplitude of the coarsening law decreases as the R_2-to-RhP transition approached, $\tilde{T}_{11} \sim a_- - a \to 0$; see Fig. 5(a) of Ref. [16]. This is in accord with the depression of this amplitude implied by our Eq. (3.11).

To summarize, the above analytic results explain the coarsening with

$$\lambda \sim t^{2/7}, \quad \xi \sim t^{4/7} \tag{3.12}$$

seen in the simulations of the rippled state [3,16]. We note however, that under some circumstances, a different coarsening with

$$\lambda \sim t^{1/3}, \quad \xi \sim t^{1/2} \tag{3.13}$$

is also seen in the rippled state simulations in Ref. [16]. In the phase diagram, such a coarsening occurs for $u_{21} \neq u_{12}$, in a subdomain of the rippled state range just below of the intensely rough subdomain of the RhP state in Fig. 3 of [16] (see the Appendix to this paper and Fig. 5 therein). For $u_{21} \neq u_{12}$, the effective free energy, invoked in deriving the coarsening in Eq. (3.12), does not exist [see Eq. (2.23) and the discussions of Eqs. (2.7)–(2.9)]. This feature itself is responsible for the existence of the buckled-rippled state and of the intensely rough RhP state [16], and apparently, it is also responsible for the existence of the rippled state subdo-

main with the coarsening behavior in Eq. (3.13). Morphology of the dislocations in this subdomain, as obtained from our simulations, is shown in Fig. 6(b) of Ref. [16]. As evidenced by the simulations, typical for these knife dislocations are long cores with the core size ξ_c comparable to the separation between dislocations ξ,

$$\xi \sim \xi_c. \tag{3.14}$$

Due to this, by invoking here Eq. (2.28c), we find

$$\xi \sim \lambda^{3/2}. \tag{3.15}$$

In the regime exhibiting these maximally elongated dislocation cores (with $\xi_c \sim \xi$), Eq. (3.15) actually replaces Eq. (3.2). Note however, that Eq. (3.15) has the form of Eq. (3.2) with (formally) setting $q=5/2$ therein. With this value of q, and $n_v=3/2$ (which applies even for $u_{21} \neq u_{12}$; see the end of Sec. II), Eqs. (3.6) and (3.7) yield

$$n_\lambda = \frac{1}{3}, \quad n_\xi = \frac{1}{2}. \tag{3.16}$$

These results explain the scaling behavior in Eq. (3.13) suggested by the simulations of Ref. [16] in the aforementioned subdomain of the rippled state range.

Next, we discuss the coarsening behavior of rectangular rippled states. Our simulations in Refs. [3,16] suggest that for these states,

$$\lambda \sim t^{1/4}, \quad \xi \sim t^{1/2}. \tag{3.17}$$

The scaling behavior in Eq. (3.17) can also be understood within the present analytic framework. To see this, we note that the dislocations of the rectangular rippled states are structurally different from the dislocations of ordinary rippled states [hence, the scaling behavior in Eq. (3.17) is unsurprisingly different from that we find for simple rippled states in Eqs. (3.12) and (3.13)]. Indeed, consider a typical dislocation of the rectangular rippled state, depicted in Fig. 4 for the case of the $R_2^{(\mathrm{rec})}$ state. The core of this dislocation is a R_1 facet having the shape of rhomb [see Fig. 4(b)]. The rhomboidal angle ψ in Fig. 4(b) is fixed by model parameters, i.e., it does not depend on the dislocation size. Due to this geometric constraint, the lateral core size ξ_c is simply proportional to λ,

$$\xi_c \sim \lambda. \tag{3.18}$$

By Eqs. (3.18) and (2.24b), we find the velocity law for the dislocations in rectangular rippled states, in the form

$$v \sim \frac{1}{\lambda^2}. \tag{3.19}$$

This dislocation velocity law corresponds to Eq. (3.4) with the velocity exponent $n_v=2$. With this value of n_v, by Eqs. (3.6) and (3.7), with again, $q=3$ channels, we find

$$n_\lambda = \frac{1}{4}, \quad n_\xi = \frac{1}{2}. \tag{3.20}$$

These results explain the scaling behavior in Eq. (3.17) that has been inferred before from the simulations of the rectangular rippled states in Refs. [3,16].

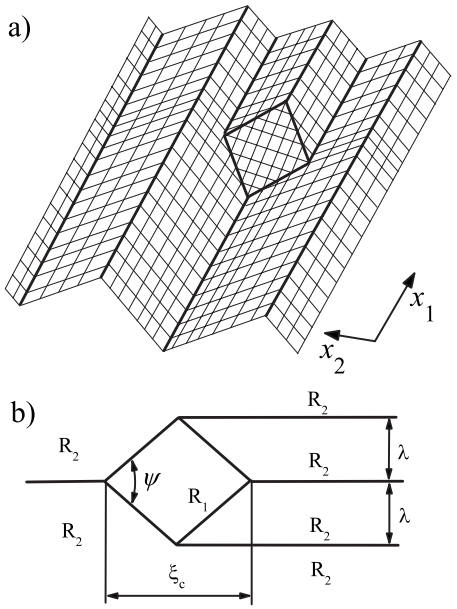

FIG. 4. (a) 3D view of a surface section around a dislocation in a rectangular rippled state $R_2^{(\mathrm{rec})}$. In (b), the dislocation is depicted in terms of the edges between facetlike surface sections seen in (a). The dislocation incorporates, in addition to the long R_2 facets, a smaller rhomboidally shaped R_1 facet at its core.

IV. SUMMARY AND DISCUSSION

In this study, we have discussed in detail the structure and dynamics of dislocations destroying perfect periodic order of the rippled surface states occurring in the epitaxial growth and erosion on (110) crystal surfaces. We have derived fundamental dislocation dynamics laws which relate the dislocation velocity to the rippled state period. We have used our dislocations velocity laws to derive the coarsening laws governing the growth of the rippled state period λ and the ripple amplitude w (surface roughness). For the simple rippled states on (110) surfaces, we have derived the coarsening law $\lambda \sim w \sim t^{2/7}$, previously guessed from the simulations [3,16]. Under some conditions however, we have found here that simple rippled states may exhibit a faster coarsening, with $\lambda \sim w \sim t^{1/3}$, also seen in the simulations [16]. We have also discussed the dislocations of the rectangular rippled surface states. For these states, we have derived the coarsening law with $\lambda \sim w \sim t^{1/4}$, in accord with the simulations [3,16]. The coarsening laws that occur at the far-from-equilibrium transition from the rippled to the rhomboidal-pyramid state have also been discussed here, as well as the crossover effects that occur in rippled states in the proximity of this transition on (110) crystal surfaces.

We end this study with a few remarks:

(1) We would like to stress that the discussions presented here have addressed the rippled and other states in the slope selection dominated regime reached at long times. In this regime, the spatial period $\lambda \sim t^{n_\lambda}$ and the interface roughness (width) $w \sim t^\beta$ must scale with the same coarsening exponent, $n_\lambda = \beta$ (as slope $\sim w/\lambda = \mathrm{const}$, due to the slope selection). In contrast to this long time regime with $n_\lambda = \beta$, in the ion erosion studies on Cu (110) [13], the selected facets of

the rippled state have not yet fully reached the preferred slope magnitude (their slope $\sim w/\lambda$ still grows within the experimentally accessible time scale). Such early time regimes are theoretically known to exhibit the coarsening exponent n smaller than β, with a typically small n [18], as was indeed observed in these experiments on the Cu (110) crystal surface [13].

(2) Throughout this study, we ignored the so-called vertical asymmetry (VA) ubiquitously present in the epitaxial growth and erosion of crystal surfaces [17]. As noted in Sec. II, the VA produces a contribution to the surface curvature current which is even under the vertical reflection $h \to -h$. VA effects were examined in detail in recent simulations [17]. They show that the VA does not alter the coarsening laws of simple rippled, rhomboidal-pyramid, and rectangular rippled states. Thus, the VA is irrelevant for these states, i.e., at long times the coarsening of these states obeys the zero VA coarsening laws discussed in this study. Nonetheless, in Ref. [17] the VA was shown to be capable of inducing novel surface states which are altered versions of the rectangular rippled states. One of them, the so-called altered $R_1^{(\mathrm{rec})}$ state, was found (from the simulations in Ref. [17]) to exhibit an enhanced coarsening with $\lambda \sim w \sim t^{0.4}$, which is significantly different from that of ordinary rectangular rippled states in Eq. (3.20). This difference is, however, unsurprising in view of significant structural differences between the $R_1^{(\mathrm{rec})}$ and the altered $R_1^{(\mathrm{rec})}$ states seen in Ref. [17]. Detailed analytic understanding of the structure and coarsening laws of the VA-induced altered $R_1^{(\mathrm{rec})}$ state remains a challenge for future theoretical works.

APPENDIX

In this Appendix, we briefly outline some details from our previous studies which are of significance for the theoretical discussions presented in this paper. References [3] and [16] show that the kinetic phase diagram of the model in Eq. (2.4) can be expressed in terms of only three dimensionless parameters defined as

$$a = \frac{r_1/\sqrt{u_{11}} - r_2/\sqrt{u_{22}}}{r_1/\sqrt{u_{11}} + r_2/\sqrt{u_{22}}},$$

$$b = \frac{u_{12}+u_{21}}{2\sqrt{u_{11}u_{22}}}, \quad c = \frac{u_{12}-u_{21}}{2\sqrt{u_{11}u_{22}}}. \tag{A1}$$

Comparisons of the theory [3,16,17] with experimental phenomenology [9,10,13] shows that the parameter a in Eq. (A1) is the most sensitive to the changes causing the transition between the two rippled states, such as the changes of deposition beam flux, beam energy, and substrate temperature. On the other hand, the parameters b and c in Eq. (A1) are less sensitive to these changes, that is, they change little across the transition. These two parameters [which depend only on the u_{ij} but not on r_i constants in the nonequilibrium surface current Eq. (2.4)] appear to depend mostly on the material used in an experiment exhibiting the transition between the rippled states R_1 and R_2.

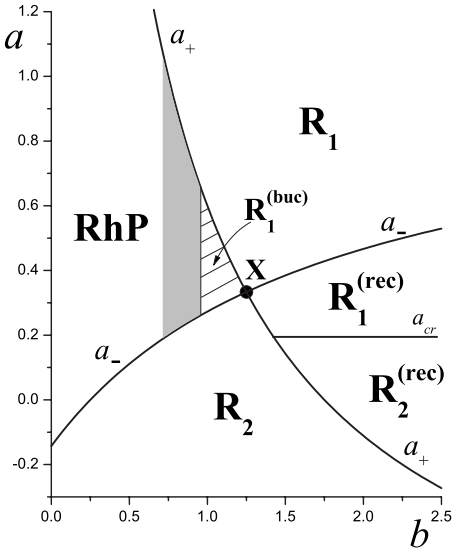

FIG. 5. Kinetic phase diagram of the model (2.4) involving simple rippled states R_1 and R_2, a rhomboidal-pyramid (RhP) state, a buckled-rippled ($R^{(\mathrm{buc})}$) state, and two rectangular rippled ($R_1^{(\mathrm{rec})}$ and $R_2^{(\mathrm{rec})}$) states. For a fixed value of c, in the (b,a) plane, the lines $a_+(b,c)$ and $a_-(b,c)$ intersect at the point X located at $b_X=\sqrt{1+c^2}$, $a_X=(\sqrt{1+c^2}-1)/c$. (The figure here is for $c=3/4$, for concreteness; any other $c>0$ would yield qualitatively the same figure.) The line $a_{\mathrm{cr}}=[\sqrt{1+(c/3)^2}-1]/(c/3)$ is the transition line between the $R_1^{(\mathrm{rec})}$ and $R_2^{(\mathrm{rec})}$ states. The intensely rough portion of the RhP state is indicated in gray. Below this region, within the R_2 state one has a portion of the rippled state domain exhibiting an enhanced roughening with the exponents given by Eq. (3.13). However, most of the rippled state domain exhibits the roughening with the exponents as in Eq. (3.12). Rectangular rippled ($R_1^{(\mathrm{rec})}$ and $R_2^{(\mathrm{rec})}$) states exhibit the roughening with the exponents as in Eq. (3.17). The phase diagram here is depicted for the case of zero vertical asymmetry. The presence of the vertical asymmetry significantly affects the rectangular rippled states (see Ref. [17]).

The kinetic phase diagram of (110) surfaces depicted in Fig. 5 is marked by two characteristic values of the control parameter a, given by

$$a_+ = \frac{1-b+c}{1+b-c}, \quad a_- = -\frac{1-b-c}{1+b+c}. \tag{A2}$$

For a fixed value of c, in the (b,a) plane, the lines $a_+(b,c)$ and $a_-(b,c)$ intersect at the point X located at $b_X=\sqrt{1+c^2}$, $a_X=(\sqrt{1+c^2}-1)/c$; see Fig. 5 here and Figs. 2 and 3 of Ref. [16]. This point separates two characteristic phase behaviors encountered in the model.

Type A behavior. For $b<b_X=\sqrt{1+c^2}$ [that is, by Eqs. (A1) and (A2) for $u_{11}u_{22}>u_{12}u_{21}$] one has $a_-(b,c)<a_+(b,c)$, and in the a parameter range

$$a_-(b,c) < a < a_+(b,c), \tag{A3}$$

R_1 and R_2 rippled phases are both unstable. There are two types of qualitatively different interface structures intervening between the two rippled phases in the range in Eq. (A3):

(i) For $b<1$, the so-called rhomboidal-pyramid (RhP) state develops [3,16]. This state is a nearly periodic structure made of four-sided pyramids, of the form

$$h(x_1,x_2) = |M_1||x_1| + |M_2||x_2|, \tag{A4}$$

within a single period $|x_1|<\lambda_1/2$, $|x_2|<\lambda_2/2$.

(ii) For $1<b<b_X$ and a in the range Eq. (A3), the so-called buckled-rippled state (R^{buc}) develops. An unusual feature of this state is that it has facets which carry nonzero surface currents, as detailed in Refs. [3] and [16].

Type B behavior. For $b>b_X=\sqrt{1+c^2}$ [that is, by Eqs. (A1) and (A2) for $u_{11}u_{22}<u_{12}u_{21}$] one has $a_-(b,c)>a_+(b,c)$, and in the a parameter range

$$a_+(b,c) < a < a_-(b,c), \tag{A5}$$

R_1 and R_2 facets are both stable. This feature gives rise to the development of the so-called rectangular rippled states $R_1^{(\mathrm{rec})}$ and $R_2^{(\mathrm{rec})}$ [3,16]. These structures have rectangular contour lines corresponding to rooflike pyramids (huts) with long rooftop edges.

Most of the phase diagram is occupied by the simple rippled states R_1 and R_2; see Fig. 5. The R_1 state occurs for $a>\max[a_+(b,c),a_-(b,c)]$. The R_2 state occurs for $a<\min[a_+(b,c),a_-(b,c)]$. In the present study, just for concreteness, we focused on the R_2 rippled state. By the above discussions, for $b<b_X$, whence $a_-(b,c)<a_+(b,c)$, the R_2 rippled state occurs for $a<a_-(b,c)$. At $a=a_-(b,c)$, the R_2 state undergoes a transition to either the rhomboidal-pyramidal state if $b<1$, or to the buckled-rippled state, however, in a typically narrow b parameter range $1<b<b_X$; see Fig. 5. In view of this, and also keeping in mind the experimental significance [13], throughout this paper we emphasized this transition mostly as the transition between the rippled state and the rhomboidal-pyramid state. Below this transition, i.e., for $a<a_-(b,c)$, the R_2 rippled state is stable. By Eqs. (A1) and (A2),

$$a_-(b,c) - a = K(-r_1 + u_{12}r_2/u_{22}) = K\tilde{T}_{11}, \tag{A6}$$

with

$$K = (2/\sqrt{u_{11}})(1 + u_{12}/\sqrt{u_{11}u_{22}})^{-1}(r_1/\sqrt{u_{11}} + r_2/\sqrt{u_{22}})^{-1} > 0. \tag{A7}$$

Note that $\tilde{T}_{11}$ in Eq. (A6) is the parameter introduced in Eq. (2.26). By Eq. (A6) and the above discussions, $\tilde{T}_{11}\sim a_- - a$ is positive within the stability range of the rippled state R_2 and it vanishes at the R_2-to-RhP transition (or at the R_2-to-R^{buc} transition, as noted above). We have been stressing this fact extensively throughout this study. Finally, we note that, in Sec. II, the a_- was written as

$$a_- = -\frac{1 - u_{12}/\sqrt{u_{11}u_{22}}}{1 + u_{12}/\sqrt{u_{11}u_{22}}}.$$

This form of a_- follows directly from Eqs. (A1) and (A2).

We note that the type A behavior (occurring in materials with $u_{11}u_{22}>u_{12}u_{21}$), which involves the formation of the rhomboidal-pyramid state intervening between rippled states, was theoretically predicted in Ref. [3] and subsequently observed in the epitaxial erosion experiments on the Rh(110) and Cu(110) surfaces [13]. On the other hand, the type B behavior (occurring in materials with $u_{11}u_{22}<u_{12}u_{21}$), with the ripple rotation transition proceeding through a multistable parameter range in which rectangular rippled states are formed [3,16,17], was observed in the experiments on the Ag(110) surface, both in the epitaxial growth [9] and in the ion beam erosion studies [10].

At the end of this Appendix, we briefly discuss the derivation of Eq. (2.9) of this paper which gives the line tension of the static edge between the R_2 facet with $(M_1=0,M_2=+M_0)$ and the R_2 facet with $(M_1=0,M_2=-M_0)$. The slope vectors of these two facets are simply opposite to each other, i.e., the angle betweeen them is 180°. Futhermore, for this edge, the interface profile is a function of one coordinate, x_2 only. Thanks to these two facts, the problem of finding the edge profile and tension reduces to that discussed in Ref. [1], in the Sec. IX therein. A simple inspection of our Eqs. (2.1)–(2.4) shows that the line tension in Eq. (2.9), for the edges in the R_2 rippled state, can be obtained directly from Eq. (72) of Ref. [1], by setting therein $2\phi=180°$, $\kappa=\kappa_{22}$, $r=r_2$, $u=u_{22}$. We finally note that the line tension for the edges in the R_1 rippled state is also of the form as in Eq. (2.9) however, with "2" in the subscripts replaced by "1."

[1] D. Moldovan and L. Golubović, Phys. Rev. E **61**, 6190 (2000).
[2] M. Siegert, Phys. Rev. Lett. **81**, 5481 (1998).
[3] L. Golubović, A. Levandovsky, and D. Moldovan, Phys. Rev. Lett. **89**, 266104 (2002).
[4] A. Levandovsky and L. Golubović, Phys. Rev. B **69**, 241402(R) (2004).
[5] For review, see J. Krug, Adv. Phys. **46**, 139 (1997); Physica A **313**, 47 (2002).
[6] J. Villain, J. Phys. I **1**, 19 (1991).
[7] T. Michely, M. Kalff, G. Comsa, M. Strobel, and K.-H. Heinig, Phys. Rev. Lett. **86**, 2589 (2001); J.-K. Zuo and J. F. Wendelken, *ibid.* **78**, 2791 (1997).
[8] J. G. Amar, Phys. Rev. B **60**, R11317 (1999).
[9] F. Buatier de Mongeot, G. Costantini, C. Boragno, and U. Valbusa, Phys. Rev. Lett. **84**, 2445 (2000). This study was the first one to report the ripple rotation transition on a (110) crystal surface, for the case of the Ag(110) surface (epitaxial growth), and to reveal an intermediary state intervening in the transition.
[10] G. Costantini, S. Rusponi, F. B. de Mongeot, C. Boragno, and U. Valbusa, J. Phys.: Condens. Matter **13**, 5875 (2001).
[11] M. Albrecht, H. Fritzsche, and U. Gradmann, Surf. Sci. **294**, 1 (1993).
[12] K. J. Caspersen, A. R. Layson, C. R. Stoldt, V. Fournee, P. A. Thiel, and J. W. Evans, Phys. Rev. B **65**, 193407 (2002).
[13] A. Molle, F. B. de Mongeot, A. Molinari, F. Xiaerding, C.

Boragno, and U. Valbusa, Phys. Rev. Lett. **93**, 256103 (2004); A. Molle, F. B. de Mongeot, A. Molinari, C. Boragno, and U. Valbusa, Phys. Rev. B **73**, 155418 (2006). This study revealed our rhomboidal-pyramid state to be present in the erosion on the Cu(110) and Rh(100) surfaces.

[14] F. Buatier de Mongeot, W. Zhu, A. Molle, R. Buzio, C. Boragno, U. Valbusa, E. G. Wang, and Z. Zhang, Phys. Rev. Lett. **91**, 016102 (2003).

[15] J. Toner and D. R. Nelson, Phys. Rev. B **23**, 316 (1981).

[16] A. Levandovsky, L. Golubović, and D. Moldovan, Phys. Rev. E **74**, 061601 (2006).

[17] A. Levandovsky and L. Golubović, Phys. Rev. E **76**, 041605 (2007).

[18] L. Golubović, Phys. Rev. Lett. **78**, 90 (1997).